

Dalton Transactions

Accepted Manuscript



This is an *Accepted Manuscript*, which has been through the Royal Society of Chemistry peer review process and has been accepted for publication.

Accepted Manuscripts are published online shortly after acceptance, before technical editing, formatting and proof reading. Using this free service, authors can make their results available to the community, in citable form, before we publish the edited article. We will replace this *Accepted Manuscript* with the edited and formatted *Advance Article* as soon as it is available.

You can find more information about *Accepted Manuscripts* in the [Information for Authors](#).

Please note that technical editing may introduce minor changes to the text and/or graphics, which may alter content. The journal's standard [Terms & Conditions](#) and the [Ethical guidelines](#) still apply. In no event shall the Royal Society of Chemistry be held responsible for any errors or omissions in this *Accepted Manuscript* or any consequences arising from the use of any information it contains.



Journal Name

ARTICLE

A Combined Experimental and Computational Study of Novel Nanocage-based Metal-Organic Frameworks for Drug Delivery

Received 00th January 20xx,

Jian-Qiang Liu,^{a*} Xue-Feng Li,^b Chu.-Ying Gu,^a Júlio C. S. da Silva,^c Amanda L. Barros,^c Severino Alves-Jr,^c Bao-Hong Li,^a Fei Ren,^{d*} Stuart R. Batten^e, Thereza A. Soares^{c*}

Accepted 00th January 20xx

DOI: 10.1039/x0xx00000x

www.rsc.org/

Three new metal organic frameworks (MOFs) with chemical formulae $[(\text{CH}_3)_2\text{NH}_2][(\text{Sm}_3(\text{L1})_2(\text{HCOO})_2(\text{DMF})_2(\text{H}_2\text{O})) \cdot 2\text{DMF} \cdot 18\text{H}_2\text{O}$ (**1**), $[(\text{Cu}_2(\text{L2})(\text{H}_2\text{O})_2) \cdot 2.22\text{DMA}$ (**2**) and $[(\text{Zn}_2(\text{L1})(\text{DMA})) \cdot 1.75\text{DMA}$ were synthesized and structurally characterized. **1** and **2** show classical **NbO**-like topology and have two types of interconnected cages. **3** exhibits uncommon **zzz** topology and has two types of interconnected cages. These MOFs can adsorb large amounts of the drug 5-fluorouracil (5-FU) and release it in a progressive way. 5-FU was incorporated into desolvated **1**, **2** and **3** with loadings of 0.40, 0.42, 0.45 g/g per gram, respectively. The drug release rates were 72%, 96% and 79% of the drug after 96 hours in **1**, 120 hours in **2** and 96 hours in **3**, respectively. Gran Canonical Monte Carlo (GCMC) simulations were performed to investigate the molecular interactions during 5-FU adsorption to the three novel materials. The GCMC simulations reproduced the experimental trend with respect to the drug load capacity of each material. It also provided a structural description of drug packing within the frameworks, helping to explain the load capacity and controlled release characteristics of the materials. 5-FU binding preferences to **1**, **2** and **3** reflect the diversity in pore types, chemistry and sizes. The calculated drug load is more related to the molecular property of accessible volume V_{acc} than to the pore size.

Introduction

Metal-organic frameworks (MOFs) have drawn considerable attention in recent years due to promising applications in gas technology, catalysis, sensors, electronic devices.^{1–8} MOFs has also been applied to biomedical storage and release of drugs in biological environments.^{9,10} These porous materials are promising candidates as drug delivery platform due to features such as large surface area, tunable pore size and shape, adjustable composition and functionalization of pore surface, and intrinsic biodegradability.^{2,10} In this scenario, Férey and co-workers have pioneered the use of MOFs for drug adsorption and release.¹¹ This concept has been expanded by the work of several other groups motivated by the development of new

procedures of synthesis for obtaining new nanostructured porous materials with high potential for drug adsorption and controlled release, and low toxicity.^{2,12–14} Rosi and co-workers have proposed the design of the denominated biomolecule-based metal-organic frameworks (bio-MOFs), where deoxyribonucleotides and amino acids are used as organic linkers and the inorganic part is composed by biocompatible metal ions.^{15,16} This class of material exhibits good performance for the encapsulation of anionic drugs. MOFs containing amino-functionalized linkers have also been synthesized for application in the transport of pro-drugs based on metallodrugs.^{17,18} Recently, it has been shown that MOFs can be produced for the incorporation and release of two different types of drugs.¹⁹ This study has shown that a Ni-based MOF (CPO-27-Ni) can concomitantly incorporate nitric oxide and RAPTA-C drugs due to the different interactions sites between the MOF and the two adsorbates. This approach has great potential of application in drug delivery for combined therapies. Despite of the progress in the synthesis, functionalization and application of biocompatible MOFs for drug delivery, there is only a limited understanding of drug adsorption and release processes at the molecular level. Such understanding requires the characterization of the three-dimensional structure and chemical interactions for MOF-drug complexes which have been constrained by experimental challenges such as the difficulties associated with the growing

^a School of Pharmacy, Guangdong Medical University, Dongguan, 523808, P. R. China. E-mail: jianqiangliu@gdmc.edu.cn

^b School of Basic Medicine, Guangdong Medical University, Dongguan, 523808, P. R. China

^c Departament of Fundamental Chemistry, Federal University of Pernambuco, Cidade Universitária 50740-560 Recife, PE, Brazil. E-mail: thereza.soares@ufpe.br

^d Department of Pharmacy, Nanfang Hospital, Southern Medical University, Guangzhou 510515, China. Email: paper_mail@126.com

^e School of Chemistry, Monash University Victoria 3800, Australia

† Footnotes relating to the title and/or authors should appear here.

Electronic Supplementary Information (ESI) available: atomic parameters and topologies for GCMC simulations, TGA curves, X-ray powder diffraction data, IR spectra and 3D representations of unit cell. CCDC 1060133-1060134 and 1061360. See DOI: 10.1039/x0xx00000x

of mono-crystals, the possibility of adsorption on multiple sites, the presence of disordered solvent molecules and so on.^{20–23}

Computational simulations can offer a unique insight into the nature of host–guest interactions at the atomic level. In the context of porous materials, the method of choice is the Grand Canonical Monte Carlo (GCMC) which has been extensively applied to simulate gas adsorption processes.^{24–28} In the grand canonical ensemble, the number of particles in the system can vary whereas the chemical potential, volume and temperature are kept constant.^{29,30} GCMC simulations generate configurational ensembles for which adsorption isotherms and isosteric heat of adsorption can be calculated and directly compared to measurements from adsorption experiments.^{24,27–29} However, the use of GCMC simulations to investigate the adsorption of large molecules to porous materials remains challenging due to the requirement of the conformational sampling and fitting of fairly large and/or flexible molecules inside tight pores. Reported modeling studies on drug-MOFs remain rather scarce. For example, David *et al.* combined computational simulations with available experimental data to describe the adsorption and release of ibuprofen in a series of MIL-based MOFs, providing thermodynamic and structural details of the process.³¹ Horcajada *et al.* used periodic Density Functional Theory (DFT) calculations to investigate the most favorable conformations and adsorption sites of ibuprofen and busulfan on MIL-53(Fe). Vasconcelos *et al.* have performed molecular docking calculations to show that doxorubicin cannot fit within the ZIF-8 cage, and favors adsorption on the material surface.³² Cunha *et al.* performed DFT calculations in combination with GCMC simulations to evaluate the uptake process of caffeine into MIL-53, MIL-100 and MIL-127 MOFs.¹³

We report here the synthesis and structural characterization of three novel MOFs with chemical formulae $[(\text{CH}_3)_2\text{NH}_2][(\text{Sm}_3(\text{L}1)_2(\text{HCOO})_2(\text{DMF})_2(\text{H}_2\text{O}))\cdot 2\text{DMF}\cdot 18\text{H}_2\text{O}]$ (**1**), $[(\text{Cu}_2(\text{L}2)(\text{H}_2\text{O}))_2]\cdot 2.22\text{DMA}$ (**2**) and $[(\text{Zn}_2(\text{L}1)(\text{DMA}))]\cdot 1.75\text{DMA}$ (**3**) ($\text{H}_4\text{L}1 = 2,6\text{-di}(3',5'\text{-dicarboxylphenyl})\text{pyridine}$, $\text{H}_4\text{L}2 = 2,5\text{-di}(3',5'\text{-dicarboxylphenyl})\text{pyridine}$). The presence of large nanocage-based pores makes these frameworks promising candidates as drug delivery platforms. Therefore, GCMC simulations were performed for the adsorption of 5-fluorouracil (5-FU). This drug was chosen as a model due to its small size and clinical relevance for the treatment of several cancer types. The GCMC simulations show that the three frameworks can adsorb large amounts of 5-FU, which have been confirmed by experimental measurements of drug release. These experiments have also shown that 5-FU is released from the three frameworks in a progressive way.

Materials and Methods

All reagents were purchased from commercial sources and used as received. IR spectra were recorded with a Perkin–Elmer Spectrum One spectrometer in the region $4000\text{--}400\text{cm}^{-1}$ using KBr pellets. TGA were carried out with a Mettler–Toledo TA 50 under dry dinitrogen flux ($60\text{mL}\cdot\text{min}^{-1}$) at a heating rate of

$5^\circ\text{C}\cdot\text{min}^{-1}$. X-ray powder diffraction (XRPD) data were recorded on a Rigaku RU200 diffractometer at 60KV, 300mA for $\text{Cu } K\alpha$ radiation ($\lambda = 1.5406 \text{ \AA}$), with a scan speed of $2^\circ/\text{min}$ and a step size of 0.02° in 2θ .

X-ray Crystallography.

Room-temperature X-ray diffraction measurements were carried out on a Bruker SMART APEX diffractometer equipped with a graphite monochromated $\text{Mo}K\alpha$ radiation ($\lambda = 0.71073 \text{ \AA}$) by using an ω -scan technique. The intensities were corrected for absorption effects by using SADABS.³⁴ The structures were solved by using *SHELXL2014*.³³ Absorption corrections were applied by using multi-non-hydrogen atoms, which were refined anisotropically. For **1** and **2**, the unit cell exhibited large regions occupied by solvent molecules. The solvent molecules could not be modeled. The SQUEEZE option in PLATON³⁵ was used to produce a set of solvent-free diffraction intensities. The nature and number of solvent molecules were established from CH&N elemental and thermogravimetric analyses. Crystallographic details and selected bond dimensions for **1–3** are listed in Tables 1 and 2. **CCDC number:** 1060133-1060134 for **1** and **2**, and 1061360 for **3**.

Synthesis

$[(\text{CH}_3)_2\text{NH}_2][(\text{Sm}_3(\text{L}1)_2(\text{HCOO})_2(\text{DMF})_2(\text{H}_2\text{O}))\cdot 2\text{DMF}\cdot 18\text{H}_2\text{O}]$ (1**).** A mixture of $\text{Sm}(\text{NO}_3)_2\cdot 6\text{H}_2\text{O}$ (0.450g, 0.1 mmol), H_4L (0.015g, 0.04 mmol) was dissolved in DMF (4mL) in a screw-capped vial. Then, five drops of HNO_3 (65%, aq) were added into the mixture. The vial was capped and placed in an oven at 110°C for 3 days. The resulting pale yellow single crystals were washed with absolute $\text{CH}_3\text{CH}_2\text{OH}$ three times to give **1**. $\text{C}_{58}\text{H}_{94}\text{N}_7\text{O}_{43}\text{Sm}_3$ (2028.45). Calcd: C, 34.34; H, 4.67; N, 4.83. Found C, 34.25.; H, 4.55; N, 4.64. IR (KBr, cm^{-1}): 3458(vs); 2026(m); 1628(m); 1435(v); 1390(v); 1269(vs); 1183(m); 1107(m); 1021(m); 917(vs); 778(vs); 715(vs); 657(vs); 454(m).

$[(\text{Cu}_2(\text{L}2)(\text{H}_2\text{O}))_2]\cdot 2.22\text{DMA}$ (2**).** A mixture of $\text{Cu}(\text{NO}_3)_2\cdot 3\text{H}_2\text{O}$ (0.055 g, 0.2 mmol), H_4L (0.021g, 0.05 mmol) was dissolved in DMA (4mL) in a screw-capped vial. Then, ten drops of HNO_3 were added into the mixture. The vial was capped and placed in an oven at 110°C for 3 days. The resulting blue single crystals were washed with absolute $\text{CH}_3\text{CH}_2\text{OH}$ three times to give **2**. $\text{C}_{29.89}\text{H}_{41}\text{Cu}_2\text{N}_{3.22}\text{O}_{12.22}$ (768.07). Calcd: C, 46.74; H, 5.38; N, 5.87. Found C, 46.35.; H, 5.27; N, 5.78. IR (KBr, cm^{-1}): 3471(vs); 2368(m); 1623(vs); 1390(vs); 1051(vs); 998(m); 770(m); 572(m).

$[(\text{Zn}_2(\text{L}1)(\text{DMA}))]\cdot 1.75\text{DMA}$ (3**).** The synthesis procedure was similar to that for **1** except that $\text{Sm}(\text{NO}_3)_2\cdot 6\text{H}_2\text{O}$ and DMF were replaced by $\text{Zn}(\text{NO}_3)_2\cdot 6\text{H}_2\text{O}$ (0.1 mmol) and DMA(4 mL). Anal. Calcd for $\text{C}_{32}\text{H}_{33.75}\text{N}_{3.75}\text{O}_{10.75}\text{Zn}_2$ (773.62), C, 49.68; H, 4.40; N, 6.79. Found C, 49.01.; H, 4.29; N, 6.55. IR (KBr, cm^{-1}): 3072(vs); 2832(m); 1644(v); 1574(vs); 1411(v); 1349(vs); 1248(vs); 783(vs); 721(vs); 636(m).

Drug Loading and Release

To load 5-fluorouracil (5-FU) into the pores of desolvated **1-3**, the dehydrated frameworks were dispersed in a 5-FU containing methanol solution (25 mL) and stirred for up to 3 days when maximum drug load was attained. These steps were followed by extensive centrifugation and sample washing with chloroform to obtain the drug-loaded frameworks. The amount of 5-FU adsorbed into the porous solids was estimated by Fourier-Transform Infrared (FTIR) and UV-Vis absorption spectroscopy at 265 nm and. Experiments were performed in quadruplicate and drug payloads 5-FU was calculated according to the equation:

$$\text{5-FU (wt\%)} = \frac{\text{5-FU(mg)}}{\text{hydrated materials(mg)}} \%$$

Amount of inclusions were loaded into a dialysis bag (MWCO = 1000), which were dialyzed against 500 mL of PBS buffer solution (pH 7.4) at room temperature. During each time interval, 1 mL of solution was taken out, and 1 mL of fresh PBS buffer was added. The adsorbed amount of 5-FU into the solids was determined by UV-Vis adsorption spectroscopy at excitation wavelength of 265 nm.

Computational Details

The adsorption process of the 5-Fluorouracil (5-FU) molecule to **1,2** and **3** was investigated using Grand Canonical Monte Carlo simulations (GCMC) at 300 K. Interactions of 5-FU with frameworks were described by a potential composed of van der Waals and Coulomb components. van der Waals interactions were treated using the Lennard-Jones (LJ) potential and atomic parameters taken from the UFF force field³⁶ (details in Support Information). The mixed LJ parameters for 5-FU/MOF and 5-FU/5FU interactions were calculated using the Lorentz-Berthelot mixing rules, and LJ interactions beyond 12 Å were neglected. Coulomb interactions were calculated using atomic partial charges obtained via the charge equilibration method (EQeq) proposed by Snurr and co-workers.³⁷ Partial charges for 5-FU molecule were calculated at B3LYP/6-311**G level of theory (see SI) via the ChelpG³⁸ method as implemented in Gaussian 09 program.³⁹ From these atomic charges, the electrostatic interactions were computed using the Ewald sum method.^{40,41} GCMC simulations were carried out with 1×10^7 equilibration steps and 2×10^7 production steps. The configuration-bias Monte Carlo method^{42,43} was used for trial MC moves involving insertion and deletion of 5-FU molecule. Trial moves related to the rotation and translation of 5-FU molecules was performed randomly. Potential maps used in configuration-biased GCMC simulations were calculated using a grid spacing of 0.1 Å and a cut off of 160 kJ mol⁻¹ for interaction energy. All MC moves included in this study were treated with equal probability. The framework was treated as rigid and vibrational and angular deformations of 5-FU molecules were neglected. All GCMC simulations were performed using the Multipurpose Simulation Code.⁴⁴ Pore size distributions (PSD), pore volume, accessible surface area and crystal density were calculated using the MC algorithm implemented in the Zeo++ program.^{45,46} Structural properties

were calculated using a charge probe of 1.2 Å of radii. Drug loading was calculated from the excess number of drug molecules. The excess number of molecules was calculated according the equation

$$n = n^{abs} - V^g \rho$$

where V^g is the pore volume of the adsorbent and ρ is the molar density of the bulk gas phase calculated by using Peng-Robinson equation of state. n^{abs} is the absolute number of molecules obtained from the GCMC simulations performed at pressure of 1 atm. Critical properties of 5-FU molecule required for the calculation of molar density of the bulk phase were taken from previously estimated values.⁴⁷ The values of critical temperature, critical pressure and critical volume used in these calculations were 1056.17 K, 58.59 bar and 248.0 cm³ mol⁻¹, respectively. The pore volume of frameworks investigated was computed using the Monte Carlo method as implemented in Zeo++ code.^{45,46}

Results and Discussion

X-ray structure of compound 1.

Although the topology of framework **1** is similar to previously reported compounds, we describe here the new structural features.⁵⁵ The structure of **1** contains Sm₃ clusters in which the metal atoms are connected by carboxylate groups from L ligands and a μ_4 formate anion (Figure 1). The L ligands in turn coordinate to three Sm₃ clusters, two *via* a single carboxylate group each, and one through two carboxylate groups (See Figure S1 for geometries around Sm centers). Hence, the ligands act as 3-connecting nodes, while the Sm₃ cluster is coordinated by eight carboxylates from six L ligands. This generates a 3D network (Figure S2) with two different 3-connecting ligand nodes (there are two crystallographically different L ligands which, in the underlying network, are also topologically different) and 6-connecting Sm₃ nodes. It has (4.6²)(4.6²)(4².6⁷.8⁶) topology.

The topology can be best thought of as interconnected cages of two types, one smaller and one larger. The smaller cage contains twelve 6-connecting nodes bridged by twelve 3-connecting nodes (one such cage is highlighted by pink bonds in Figure 2(a)). Notably, the cage contains a “belt” of four 4-membered rings around the middle. These 4-membered rings are defined by two 3-connected and two 6-connected nodes, which are connected to each other by sharing their 6-membered nodes. Two of the 4-membered rings contain one type of 3-connecting node (light green in the Figure (2a)), while the other contains the other type of 3-connecting node (dark green in the Figure 2(a)). This belt is then capped by two more 4-membered rings (containing the light green 3-connecting nodes) which are held in place by connections between their 6-connecting nodes and the light green nodes of the belt, and by bonds from both the dark green nodes of the belt and the light green nodes of the capping rings to additional 6-connecting nodes.

Therefore, each one of the small cages contains six 4-membered rings, four in a central belt and two capping above

and below this belt, in a distorted octahedral arrangement. These cages are connected to each other via the sharing of the four rings with the light green nodes between adjacent cages, meaning that each cage is connected to four neighbors. As adjacent cages are orientated approximately perpendicular to each other (Figure 2(a)), the cages connects together in a **NbO**-type fashion (Figure 2(b)). This generates a larger cavity (blue spheres in Figure 2(b)), which corresponds to the larger cage of the underlying 3,3,6-connected net mentioned earlier. The larger cage, highlighted by the blue bonds in Figure 2(a), contains six 4-membered rings joined together by connections between 3-connecting nodes of one ring to 6-connecting nodes of adjacent rings, and has the same topology as the sodalite cage. Notably, the 3-connecting nodes in this larger cage are all exclusively of the dark green variety.

X-ray structure of compound 2.

The structure of **2** is similar to that of the compound $\{[(\text{Cu}_2(\text{L}2)(\text{H}_2\text{O})_2)\cdot x\text{solvent}]_n\}$ that has been reported by Champness et al.⁴⁸ The structure of **2** contains dinuclear Cu_2 clusters displaying the classic copper acetate motif, in which pairs of Cu metals are bridged by carboxylate groups from four separate ligands (Figure 3). The five-coordinate geometries of the metals are completed by coordinated water ligands. The L ligands in turn coordinate to four separate Cu_2 dimers. The 3D network can be simplified by treating both the Cu_2 dimers and L2 ligands as 4-connecting nodes. This reduces the structure to a network with **NbO**-like topology (Figure 4); both the Cu_2 dimers and L ligands act as the square planar nodes (all four carboxylate groups of the ligand are close to coplanar).

X-ray structure of compound 3.

The structure of **3** contains linear Zn_4 clusters bridged by L1 ligands; all clusters and all L1 are equivalent. The Zn_4 cluster contains two different Zn atoms (Figure 5(a)). The central Zn atoms are 5-coordinate and bridged to each other by two L carboxylate groups. The two outer Zn atoms are then each connected to a central Zn via three bridging L1 carboxylate groups. The coordination spheres of the tetrahedral outer Zn atoms are then completed by a disordered DMA ligand. Each Zn_4 cluster is thus coordinated by eight carboxylate groups from six L1 ligands. Each L1 is, in turn, coordinated to three Zn_4 clusters, once each to two and twice to the third (Figure 5(b)). Based on this connection, an open framework with 3D infinite intersected channels was formed (Figure 5(c)). The dimensions of the largest channels are approximately $5.1 \times 5.6 \text{ \AA}$ along the *c* axis. This generates a 3,6-connected net with **zzz**-like topology (Figure 6). The net is closely related to the common rutile net (**rtl**), which has the same Schläfli symbol $((4.6^2)_2(4^2.6^{10}.8^3))$, however it contains two different types of channels. One is topologically the same as those in the rutile net (highlighted in pink in Figure 6), where opposing 6-membered rings are connected directly to each other, while in the other (highlighted in blue) the 6-membered rings spiral along the channel (there are equal numbers of helical channels of opposite handedness).

Drug Adsorption Measurements

The framework structure of **1** is anionic with H_2O and $(\text{CH}_3)_2\text{NH}_2^+$ cation (the product of DMF decomposition) as well as DMF residing in the channels as shown by elemental analysis, thermogravimetric analysis and the consideration of charge balance. The TGA data (Figure S3) for **1** reveal a weight loss of 20.3% from room temperature to $240 \text{ }^\circ\text{C}$, corresponding to the loss of the free DMF and water molecules (ca. 21.3%). The as-synthesized blue-green crystalline samples of **2** lose solvent rapidly over $25\text{--}110 \text{ }^\circ\text{C}$, resulting in a deep purple-blue crystalline material. Desolvated **2** can be stabilized until $115 \text{ }^\circ\text{C}$. The total observed weight losses based on the removal of DMA molecules in the first step was around 16.6% (cal. 17.1%) from 30 to $115 \text{ }^\circ\text{C}$. For **3**, in the first step from 31.5 to $190 \text{ }^\circ\text{C}$, the observed weight loss is 26.5 %, which corresponds to the release of DMA molecules (cal. 28.9%).

The unusually large cages of the three porous structures led us to examine its drug release capability. 5-FU was selected because of its size, which was small enough to be incorporated into the cavity of **1-3**. Before its use as a drug delivery carrier, Samples **1-3** were activated (see Figure S4). Then, adsorption of anticancer 5-FU was carried out by impregnating **1-3** under stirring in 5-FU containing ethanol solutions. As evidenced by PXRD, 5-FU containing sample maintains its crystallinity (Figure S4), thus, the drug encapsulation did not alter the structure of these materials. It suggests that a slight shrinkage/swell of the structures have taken place after removal of solvent molecules or encapsulation of drug molecules. The slight shrinkage of the structure may cause the disappearance of the strong diffraction peak at low angle reflections in **1** and **3**.^{2b} This was confirmed by N_2 adsorption analyses showing that the BET surface area significantly decrease upon drug molecules loading (see Supplementary Information Figure S5)^{51,52}. Incorporation of the drug molecule during adsorption process has been also confirmed by Fourier transformed infrared spectroscopy (FTIR) (Figure S6). The characteristic peaks of --O--C--O-- groups between 1660 and 1355 cm^{-1} are observed. The adsorption band at about 1240 cm^{-1} may be due to fluorine atom on the ring. The absorption bands in the $820\text{--}550 \text{ cm}^{-1}$ regions may be assigned to the C–F deformations⁴⁹. Furthermore, the very strong and broad absorption band at ca. $3300\text{--}4000 \text{ cm}^{-1}$ should be derived from OH stretching (maybe mixing with N–H band) because of the existence of water molecules in the porous materials.

UV–vis absorption spectroscopy has been used to determine the effective storage capacity (see Supplementary Information). To reach a maximal drug loading, 5-FU to porous solid relative ratio and contact time were tested. After the trivial tests, the best results were achieved when **1'-3'** were soaked for 3 days in a 20 mL ethanol solution with a 5-FU to **1'-3'** weight ratio of 1:3. 5-FU was incorporated into **1'-3'** with loadings of 0.40, 0.42, 0.45 g/g, respectively. 5-FU loading into **1'** is a little lower than that for $\{(\text{NH}_2(\text{CH}_3)_2)[(\text{Zn}(\text{TATA})_{2/3}] \cdot 3\text{DMF} \cdot \text{H}_2\text{O}\}_n$ as reported by Su and co-workers, but it is higher than that of

Cu(pi)-PEG5k polymer.^{49,50} However, 5-FU loading into **2** is higher than that of the aforementioned two compounds.

Drug release experiments were taken by dialyzing the drug-loaded **1-3'** in the PBS buffer solution (PBS = phosphate buffered saline pH 7.4) at 37 °C.⁵³ PXRD performed before and after 5-FU release shows that the crystal structure remains basically the same after the drug delivery (Fig.S4). As shown in Fig. 7, the drug release rates were 72%, 96% and 79% of drug release after 96 hours in **1'**, 120 hours in **2'** and 96 hours in **3'**, respectively. In **1'**, three stages related to the drug release could be distinguished. Around 31% of the loaded drug was released during the initial burst release (24 hours). After that, there is a much flatter release curve up to 48 hours. However, for **2'**, around 45% of the loaded drug was released during the initial burst release (24 hours) and 51% was released in the latter two stages. As to **3**, it has the similar drug releasing behavior with **2**. Around 41% of the loaded drug was released during the initial burst release (24 hours). As mentioned above, two different size of nanoscale cage exist in **1-3**. The windows of them in **1** are 4.4×4.1 and 5.5×5.0 Å (see Figure S2), while the windows of them in **2** are 4.2×4.6 and 5.8×7.3 Å and are in **3** 4.3×4.5 and 6.4×7.8 Å (see Figure S7). Thus, only one window is larger than the size of the drug molecule (5.3×5.0Å) in **1-3**. For each type cage from **1-3**, two circumstances may occur for the guest. For those drug molecules approaching the pores, the forces are dominated by the host-guest interactions from weak interactions (such as hydrogen bonds and packing interactions) between 5-FU and the skeleton of organic ligand. Therefore, the strength of the force relies on the size of the cages and chemical feature of pores. For those drug molecules far away from the pores, the forces are mainly from intermolecular interactions between 5-FU molecules. Based on above-mentioned structural distinctions, the windows of **2-3** are larger than that of compound **1**, which could be related to different loading content. Furthermore, considering the difference in window size of the larger cages in **1** and **2**, 5-FU located close to the pores of larger cages would be released preferentially with respect to those hosted into the smaller cages, which also verify different release characteristic. The host-guest interactions are further addressed *via* computational simulations of 5-FU adsorption to the frameworks. As mentioned above, the drugs from the three inclusions do not release completely, the release of the residual ~10-20% took as long as 4 d. This could be attributed to host-guest interactions between drug molecules and the skeleton (e. g., interactions between an amine group of 5-FU and the coordinative unsaturated metal center Sm/Cu/Zn in the frameworks, and π - π packing interactions between rings of 5-FU and the organic part of the frameworks)^{2a}.

Computational Simulations of 5-FU Adsorption

The amount of drug per porous material or drug loading is one of the main quantities of interest in the use of MOFs for controlled drug release. We have used GCMC simulations to investigate the adsorption of 5-FU to **1**, **2** and **3** at the molecular level. These simulations were used to determine the preferential binding sites of the 5-FU in the porous materials, to estimate

the maximum drug adsorption capacity of each material, and to propose a molecular mechanism for drug adsorption and release.

Selected structural parameters were calculated from the atomic coordinates of the three MOFs (Table 3). Structural features and the chemical nature of the pores are two important factors related with the capacity of a given material adsorb molecules. Structural details about porous materials can be obtained from the analysis of the pore size distribution (PSD), which gives information about the amount of void space exists within a certain pore sizes or the porosity of a given material (Figure 8). As can be observed, all three frameworks show distinct pore morphologies with varying pore distribution sizes (Figure 8). **1** exhibits a bimodal distribution of pore sizes (Figure 9) whereas **2** shows a pseudo-unimodal pattern (Figure 10). **3** presents two well defined pores. The smaller pore has a cylindrical shape with a diameter of ca. 10.3 Å where the Zn²⁺ cations are easily accessible to interact with 5-FU. The larger pore has a squared shape with a diameter of ca. 12.3 Å where the metallic ion is made less exposed by the presence of coordinating carboxylate groups from the organic linker (Figure 11). The X-ray structure of the **2** shows the presence of one microporous windows between the main pores (Figure 10). Only the main pore (~ 6.4 Å) is large enough to fit 5-FU (Figure 8). The **1** has also two pores with different dimensions (ca. 9.7 Å and 16.14 Å), but similar chemical environment (Figure 9). Pairs of organic linkers are positioned along the extension of both pore channels such as gates, which may hinder the entry/exit of 5-FU. The two pores differ in what concerns the horizontal (D_{\max} 9.7 Å) or vertical (D_{\max} 16.14 Å) placement of such gates (Figure 8). Hence, the set of crystallographic and PSD data shows more intricate pore morphologies and volume voids for **1** and **2**.

GCMC simulations were performed to gain insight into the adsorption mechanism of 5-FU to **1**, **2**, and **3**. Among others information, the analysis of configurations generated from GCMC simulations can provide details about the siting bind location of the drug molecules within the frameworks pores. Regarding to adsorption process of 5-FU to **3**, our results suggest that the binding of 5-FU to **3** should occurs in two steps. Initially 5-FU molecules fill up the larger pore, forming well-structured aggregates (Figure 11). Once the larger pores are occupied, 5-FU molecules bind to the smaller pore albeit in much smaller numbers (Figure 11). The nature of the interactions between of 5-FU and **3** governs such binding pattern. In the larger pore, van der Waals interactions are the major forces driving 5-FU aggregation and its interaction with the aromatic rings in the organic linker. In contrast, electrostatic interactions between 5-FU molecules and Zn²⁺ cations are the major binding factor in the smaller pore. In the latter, 5-FU molecules do not form aggregates, and the pore volume is only partially filled with drug molecules (Figure 11). 5-FU molecules adsorbs unspecifically to mesopores in **1**, following a single binding regime. Likewise for **2**, this has only one pore type large enough to incorporate 5-FU molecules. In both frameworks, 5-FU binds predominantly through electrostatic

interactions with the metals ions and the carboxylate groups from the organic linkers (Figures 9 and 10).

Two common features emerged from the GCMC simulations of 5-FU adsorption to **1**, **2**, and **3**. First, different 5-FU molecules make extensive intermolecular interactions upon confinement into the respective pores (Figures 9-11). These interactions result from the presence of four hydrogen donor-acceptor sites in the pyrimidine group, which allows for a highly packed and structured arrangement of 5-FU molecules within pores. Second, the three frameworks exhibit an analogous adsorption capacity for 5-FU molecules despite their rather distinct structures and pore dimensions (Table 3). This is shown by computer simulations and experimental measurements (the deviation between experimental and theoretical loading values will be discussed afterwards). How structurally distinct frameworks exhibit nearly undistinguishable 5-FU load capacity?

An approach to understand the drug loading behavior of porous materials is to relate it to structural properties (*e.g.* surface area, density of material, pore size and available pore volume) (Table 3). **2** is the densest material ($\rho_{\text{cryst}} = 1.19 \text{ g cm}^{-3}$), has the smallest accessible volume per gram of material ($V_{\text{acc}} = 0.096 \text{ cm}^3 \text{ g}^{-1}$) and the smallest pore size structure ($D_{\text{max}} = 6.40 \text{ \AA}$) among the frameworks considered here. It has also the largest accessible surface area A_{asa} . Comparatively, **1** is less dense ($\rho_{\text{cryst}} = 1.07 \text{ g cm}^{-3}$), has the smallest accessible surface area ($A_{\text{asa}} = 1815.3$) of the three frameworks, a larger accessible volume per gram of material ($V_{\text{acc}} = 0.272 \text{ cm}^3 \text{ g}^{-1}$), and the largest pore dimension ($D_{\text{max}} = 16.14 \text{ \AA}$). **3** is the material with the lowest crystal density ($\rho_{\text{cryst}} = 0.95 \text{ g cm}^{-3}$), the highest accessible volume per gram ($0.366 \text{ cm}^3 \text{ g}^{-1}$), the second larger accessible surface area ($A_{\text{asa}} = 2136.1 \text{ m}^2 \text{ g}^{-1}$). In the GCMC simulations of **2**, 5-FU binds inside the pore but also onto the framework surface (Figure 10). In this material, the pore dimension restricts the number of drug molecules that can be accommodated across the pore diameter, and imposes a linear arrangement of these molecules along the pore channel. This is in contrast to simulations of **1** and **3**, which have lower density, smaller surface area and larger accessible volume compared to **2**. In these frameworks, 5-FU binds exclusively within the respective pores (Figures 9 and 11).

A tentative molecular mechanism for the release of 5-FU from **1-3** is proposed based on the comparison between the GCMC simulations and the drug release profiles for these materials (Figure 7). It should be mentioned that GCMC simulations does not offer direct information on time-dependent phenomena. Hence, the proposed molecular mechanism relies solely on the Boltzmann-averaged occupation rates of 5-FU with respect to different pores in the same framework. Three different stages are distinguished in the drug delivery profile for **1** and **3**. The first stage corresponds to the initial burst when there is a rapid release of the drug. At this stage, ca. 20% to 25% of 5-FU is released in 12h from **3** and **1**, respectively (Figure 7). In the remaining stages, 5-FU is progressively released as shown by the flattening of the profile curves. The drug release profiles of **1** and **3** are nearly undistinguishable during the first stage of the process (Figure 7). Afterwards, 5-

FU is released from **1** at slower rates compared to **3**. In **3**, 5-FU molecules in the form of aggregates interact with the large pore mainly via van der Waals interactions and with the small pore through electrostatic interactions with the metallic center (Figure 11). The different nature of these interactions implies that 5-FU will be released first, and in sizeable amounts, from the large pore (via disruption of the short ranged van der Waals interactions) and then from the smaller pore at slower rates. In the case of **1**, 5-FU bound outside the pore gate can readily diffuse into the bulk solution as opposed to molecules inside the pore whose diffusion will be hindered or reduced by the gate (linkers) (Figure 9). Compound **2** exhibits a rather distinct drug release profile from those measured for **1** and **3** (Figure 7). In fact, its release curve shows two regimes: an initial burst in the first 12h, followed by the uniform and steady release of 5-FU. Based on the GCMC simulations, the initial burst can be associated to the excess of 5-FU molecules adsorbed on the framework surface. The subsequent release stages can be connected to the slower diffusion of 5-FU molecules from **2** pores. Due to the small pore size of **2**, 5-FU molecules are arranged in a linear manner along the pore channel (Figure 10). Such arrangement can lead to the steady release of 5-FU observed in the drug release measurements (Figure 7).

It should be mentioned that the calculated loading values are on average 40% lower than the experimentally measured ones (Table 3). Differences between experimental and calculated values within the same order of magnitude have been previously reported from adsorption studies involving different frameworks and drugs.^{31,13} The discrepancy between calculated and experimental values can arise from diffusional issues during the pore filling process by drug molecules, which cannot be captured directly from GCMC simulations. It can also result from the inaccuracies in the experimental loading measurements. The experimental protocol relies on certain assumptions (*e.g.* drug solubility, porous material activation and solvent-drug competition for binding sites in the material) that are not easily ascertained. Further, experimental measurements are made indirectly from the excess of drug in solution, whereas the GCMC simulations quantify the number of drug molecules bound in pores of the material. Despite these limitations, our theoretical results indicate that the GCMC method reproduce drug loading values in MOFs within the same order of magnitude of experimental values while offering a microscopic, structure-based perspective of the adsorption process.

Conclusions

The present study reports on the experimental and computational characterization of three novel MOFs as drug delivery platforms. The elucidation of the respective 3D structures revealed the presence of large nanocage-based pores. This structural feature was explored via GCMC simulations with the goal to identify a suitable drug for incorporation. GCMC simulations suggested that the anti-cancer drug 5-fluorouracil (5-FU) could adsorb to the three frameworks in high loads. The computational estimates were confirmed by

drug adsorption experiments: 5-FU can be incorporated into desolvated **1**, **2** and **3** with loadings of 0.40, 0.42, 0.45 g/g, respectively. Furthermore, 5-FU is released from these frameworks in a progressive manner with release rates of 72%, 96% and 79% after 96 hours in **1**, 120 hours in **2** and 96 hours in **3**, respectively. Our findings show that the combined experimental-computational approach is a powerful strategy for the efficient identification and incorporation of bioactive compounds in novel porous materials.

Acknowledgements

This work was partially supported by grants from the National Natural Science Foundation of China (Grant 21201044), the Chinese Training Plan of Guangdong Province Outstanding Young Professors in Higher Education Institutions (Grant YQ2013084), the Brazilian National Counsel of Technological and Scientific Development, CNPq (Grant PVE-400193/2013-2) and CAPES (Grant BioMol-230380046302014-35). JCSS acknowledges post-doctoral fellowship from CNPq. TAS and SAJ are productivity fellows in research from CNPq. Prof. S. W. Ng is acknowledged for the refinement of structural data. The experimental measurements have been carried out by the Chinese team and the computational simulations by the Brazilian team.

Notes and references

- R. B. Getman, Y.-S. Bae, C. E. Wilmer and R. Q. Snurr, *Chem. Rev.*, 2012, **112**, 703–723.
- (a) P. Horcajada, R. Gref, T. Baati, P. K. Allan, G. Maurin, P. Couvreur, G. Férey, R. E. Morris and C. Serre, *Chem. Rev.*, 2012, **112**, 1232–1268; (b) V. Agostoni, T. Chalati, P. Horcajada, H. Willaime, R. Anand, N. Semiramoth, T. Baati, S. Hall, G. Maurin, H. Chacun, K. Bouchemal, C. Martineau, F. Taulelle, P. Couvreur, C. Rogez-Kreuz, P. Clayette, S. Monti, C. Serre and R. Gref, *Adv. Healthcare Mater.*, 2013, **2**, 1630–1637.
- (a) L. E. Kreno, K. Leong, O. K. Farha, M. Allendorf, R. P. Van Duyne and J. T. Hupp, *Chem. Rev.*, 2012, **112**, 1105–1125; (b) S. H. Li, M. L. Han, G. Z. Liu, L. F. Ma and L. Y. Wang, *RSC Adv.*, 2015, **5**, 17588–17591; (c) G. L. Li, G. Z. Liu, L. F. Ma, L. X. Xin, X. L. Li and L. Y. Wang, *Chem. Comm.*, 2014, **50**, 2615–2617.
- J.-R. Li, J. Sculley and H.-C. Zhou, *Chem. Rev.*, 2012, **112**, 869–932.
- M. P. Suh, H. J. Park, T. K. Prasad and D.-W. Lim, *Chem. Rev.*, 2012, **112**, 782–835.
- M. Yoon, R. Srirambalaji and K. Kim, *Chem. Rev.*, 2012, **112**, 1196–1231.
- K. Sumida, D. L. Rogow, J. A. Mason, T. M. McDonald, E. D. Bloch, Z. R. Herm, T.-H. Bae and J. R. Long, *Chem. Rev.*, 2012, **112**, 724–781.
- C. Wang, T. Zhang and W. Lin, *Chem. Rev.*, 2012, **112**, 1084–1104.
- P. Horcajada, T. Chalati, C. Serre, B. Gillet, C. Sebrie, T. Baati, J. F. Eubank, D. Heurtaux, P. Clayette, C. Kreuz, J.-S. Chang, Y. K. Hwang, V. Marsaud, P.-N. Bories, L. Cynober, S. Gil, G. Férey, P. Couvreur and R. Gref, *Nat Mater.*, 2010, **9**, 172–178.
- S. Keskin and S. Kızılel, *Ind. Eng. Chem. Res.*, 2011, **50**, 1799–1812.
- G. Férey, C. Mellot-Draznieks, C. Serre, F. Millange, J. Dutour, S. Surblé and I. Margiolaki, *Science*, 2005, **309**, 2040–2042.
- R. C. Huxford, J. Della Rocca and W. Lin, *Curr. Opin. Chem. Biol.*, 2010, **14**, 262–268.
- D. Cunha, M. Ben Yahia, S. Hall, S. R. Miller, H. Chevreau, E. Elkaïm, G. Maurin, P. Horcajada and C. Serre, *Chem. Mater.*, 2013, **25**, 2767–2776.
- W. J. Rieter, K. M. Pott, K. M. L. Taylor and W. Lin, *J. Am. Chem. Soc.*, 2008, **130**, 11584–11585.
- J. An, S. J. Geib and N. L. Rosi, *J. Am. Chem. Soc.*, 2009, **131**, 8376–8377.
- C.-L. Chen and N. L. Rosi, *Angew. Chemie Int. Ed.*, 2010, **49**, 1924–1942.
- K. M. L. Taylor-Pashow, J. Della Rocca, Z. Xie, S. Tran and W. Lin, *J. Am. Chem. Soc.*, 2009, **131**, 14261–14263.
- J. Della Rocca, D. Liu and W. Lin, *Acc. Chem. Res.*, 2011, **44**, 957–968.
- S. Rojas, P. S. Wheatley, E. Quartapelle-Procopio, B. Gil, B. Marszalek, R. E. Morris and E. Barea, *CrystEngComm*, 2013, **15**, 9364–9367.
- F. Gandara and T. D. Bennett, *IUCrJ*, 2014, **1**, 563–570.
- G.-L. Li, G.-Z. Liu, L.-F. Ma, L.-Y. Xin, X.-L. Li and L.-Y. Wang, *Chem. Commun.*, 2014, **50**, 2615–2617.
- J. L. C. Rowsell, E. C. Spencer, J. Eckert, J. A. K. Howard and O. M. Yaghi, *Science*, 2005, **309**, 1350–1354.
- Y. Kubota, M. Takata, R. Matsuda, R. Kitaura, S. Kitagawa, K. Kato, M. Sakata and T. C. Kobayashi, *Angew. Chemie Int. Ed.*, 2005, **44**, 920–923.
- T. Düren, L. Sarkisov, O. M. Yaghi and R. Q. Snurr, *Langmuir*, 2004, **20**, 2683–2689.

ARTICLE

Journal Name

25. K. S. Walton, A. R. Millward, D. Dubbeldam, H. Frost, J. J. Low, O. M. Yaghi and R. Q. Snurr, *J. Am. Chem. Soc.*, 2008, **130**, 406–407.
26. Z. Xiang, D. Cao, J. Lan, W. Wang and D. P. Broom, *Energy Environ. Sci.*, 2010, **3**, 1469–1487.
27. R. Babarao and J. Jiang, *Langmuir*, 2008, **24**, 6270–6278.
28. Q. Yang, C. Zhong and J.-F. Chen, *J. Phys. Chem. C*, 2008, **112**, 1562–1569.
29. T. Duren, Y.-S. Bae and R. Q. Snurr, *Chem. Soc. Rev.*, 2009, **38**, 1237–1247.
30. D. Dubbeldam, A. Torres-Knoop and K. S. Walton, *Mol. Simul.*, 2013, **39**, 1253–1292.
31. M. C. Bernini, D. Fairen-Jimenez, M. Pasinetti, A. J. Ramirez-Pastor and R. Q. Snurr, *J. Mater. Chem. B*, 2014, **2**, 766–774.
32. I. B. Vasconcelos, T. G. da Silva, G. C. G. Militao, T. A. Soares, N. M. Rodrigues, M. O. Rodrigues, N. B. da Costa, R. O. Freire and S. A. Junior, *RSC Adv.*, 2012, **2**, 9437–9442.
33. G. G. M. Sheldrick; SHELXTL NT Version 5.1. Program for Solution and refinement of Crystal Structures, University of Göttingen, 1997.
34. Bruker AXS, SAINT Software reference Manual, Madison, WI, 1998.
35. A. L. Spek, *J. Appl. Crystallogr.*, 2003, **36**, 7–13.
36. A. K. Rappe, C. J. Casewit, K. S. Colwell, W. A. Goddard and W. M. Skiff, *J. Am. Chem. Soc.*, 1992, **114**, 10024–10035.
37. C. E. Wilmer, K. C. Kim and R. Q. Snurr, *J. Phys. Chem. Lett.*, 2012, **3**, 2506–2511.
38. C. M. Breneman and K. B. Wiberg, *J. Comput. Chem.*, 1990, **11**, 361–373.
39. W. C. Gaussian 09, Revision C.01, G. M. J. Frisch, W. Trucks, H. B. Schlegel, G. E. Scuseria, M. A. Robb, J. R. Cheeseman, G. Scalmani, V. Barone, B. Mennucci, G. A. Petersson, H. Nakatsuji, M. Caricato, X. Li, H. P. Hratchian, A. F. Izmaylov, J. Bloino, G. Zheng and D. J. F. Sonnenberg, J. L. M. Hada, M. Ehara, K. Toyota, R. Fukuda, J. Hasegawa, M. Ishida, T. Nakajima, Y. Honda, O. Kitao, H. Nakai, T. Vreven, J. A. Montgomery, Jr., J. E. Peralta, F. Ogliaro, M. Bearpark, J. J. Heyd, E. Brothers, K. N. Kudin, V. N. Staroverov, R. Kobayashi, J. Normand, K. Raghavachari, A. Rendell, J. C. Burant, S. S. Iyengar, J. Tomasi, M. Cossi, N. Rega, J. M. Millam, M. Klene, J. E. Knox, J. B. Cross, V. Bakken, C. Adamo, J. Jaramillo, R. Gomperts, R. E. Stratmann, O. Yazyev, A. J. Austin, R. Cammi, C. Pomelli, J. W. Ochterski, R. L. Martin, K. Morokuma, V. G. Zakrzewski, G. A. Voth, P. Salvador, J. J. Dannenberg, S. Dapprich, A. D. Daniels, Ö. Farkas, J. B. Foresman, J. V. Ortiz, J. Cioslowski, and D. J. Fox; 2009.
40. M. P. Allen and D. J. Tildesley, *Computer Simulation of Liquids (Oxford Science Publications) SE - Oxford science publications*, Oxford University Press, 1989.
41. H. Dufner, S. M. Kast, J. Brickmann and M. Schlenkrich, *J. Comput. Chem.*, 1997, **18**, 660–676.
42. M. N. Rosenbluth and A. W. Rosenbluth, *J. Chem. Phys.*, 1955, **23**, 356.
43. J. I. Siepmann and D. Frenkel, *Mol. Phys.*, 1992, **75**, 59–70.
44. A. Gupta, S. Chempath, M. J. Sanborn, L. A. Clark and R. Q. Snurr, *Mol. Simul.*, 2003, **29**, 29–46.
45. T. F. Willems, C. H. Rycroft, M. Kazi, J. C. Meza and M. Haranczyk, *Microporous Mesoporous Mater.*, 2012, **149**, 134–141.
46. R. L. Martin, B. Smit and M. Haranczyk, *J. Chem. Inf. Model.*, 2012, **52**, 308–318.
47. F. J. Ramos, R. Mazarro, A. de Lucas Martínez and J. F. Rodríguez, in *STUDY OF THE PHASE EQUILIBRIUM IN BINARY SYSTEMS: ANTICANCER DRUG-CARBON DIOXIDE. 10th International Symposium on Supercritical Fluids (ISSF)*, 2012.
48. X. Lin, J. Jia, X. Zhao, K. M. Thomas, A. J. Blake, G. S. Walker, N. R. Champness, P. Hubberstey and M. Schröder, *Angew. Chemie Int. Ed.*, 2006, **45**, 7358–7364.
49. C.-Y. Sun, C. Qin, C.-G. Wang, Z.-M. Su, S. Wang, X.-L. Wang, G.-S. Yang, K.-Z. Shao, Y.-Q. Lan and E.-B. Wang, *Adv. Mater.*, 2011, **23**, 5629–5632.
50. D. Zhao, S. Tan, D. Yuan, W. Lu, Y. H. Rezenom, H. Jiang, L.-Q. Wang and H.-C. Zhou, *Adv. Mater.*, 2011, **23**, 90–93.
51. B. Liu, W. P. Wu, L. Hou and Y. Y. Wang, *Chem. Commun.*, 2014, **50**, 8731–8734.
52. X. Lin, J. H. Jia, X. B. Zhao, K. M. Thomas, A. J. Blake, G. S. Walker, N. R. Champness, P. Hubberstey and M. Schröder, *Angew. Chem. Int. Ed.*, 2006, **45**, 7358–7364.
53. T. Wang, F. Chai, Q. Fu, L. Zhang, H. Liu, L. Li, Y. Liao, Z. Su, C. Wang, B. Duan and D. Ren, *J. Mater. Chem.*, 2011, **21**, 5299–5306.



Journal Name

ARTICLE

Table 1. Crystal data and structure refinement information for novel framework structures.

Complex	1	2	3
Empirical formula	C ₅₈ H ₉₄ N ₇ O ₄₃ Sm ₃	C _{29.89} H ₄₁ Cu ₂ N _{3.22} O _{12.22}	C ₃₂ H _{33.75} N _{3.75} O _{10.75} Zn ₂
Formula mass	2028.45	768.07	773.62
Crystal system	cubic	trigonal	tetragonal
Space group	<i>I</i> <i>m</i> -3	<i>R</i> -3 <i>m</i>	<i>P</i> 4/ <i>n</i>
<i>a</i> [Å]	38.3513(17)	18.6342(14)	27.4541(15)
<i>b</i> [Å]	38.3513(17)	18.6342(14)	27.4541(15)
<i>c</i> [Å]	38.3513(17)	37.709(3)	9.7375(5)
<i>α</i> [°]	90	90	90
<i>β</i> [°]	90	90	90
<i>γ</i> [°]	90	120	90
<i>V</i> [Å ³]	56408(8)	11339.7(19)	7339.4(6)
<i>Z</i>	24	9	8
<i>d</i> _{calcd} [g cm ⁻³]	1.433	1.012	1.400
<i>F</i> (000)	24504	3588	3184
Reflections collected	175427	23422	69414
<i>R</i> _(int)	0.0297	0.0529	0.0394
<i>R</i> ₁ , <i>wR</i> ₂ [<i>I</i> > 2σ(<i>I</i>)]	0.0577, 0.1479	0.0359, 0.0950	0.0608, 0.1437
<i>R</i> ₁ , <i>wR</i> ₂ (all data)	0.0756, 0.1699	0.0523, 0.1022	0.0818, 0.1552
<i>GOF</i> on <i>F</i> ²	1.079	0.955	1.093

Table 2. Selected bond distances (Å) and angles (°) of structures 1-3

Structure 1			
Sm1-O1	2.330 (8)	Sm1 - O8	2.331 (8)
Sm1-O1w	2.520 (18)	Sm1-O10	2.579 (6)
Sm1-O12	2.590 (2)	Sm1 - O11	2.61 (2)
Sm2-O7	2.351 (7)	Sm2 - O2	2.371 (7)
Sm2- O10	2.413 (4)	Sm2 - O6	2.423 (7)
Sm2- O9	2.433 (6)	Sm2 - O5	2.433 (7)
Sm2 -O3	2.444 (7)	Sm2 - O4	2.459 (8)
O1 - Sm1 - O1	78.5 (4)	O1- Sm1- O8	77.7 (4)
O8 - Sm1 - O8	124.2 (6)	O1- Sm1- O1w	136.1 (3)
O10 - Sm1 - O12	149.6 (3)	O7- Sm2- O2	86.4 (2)
O2 - Sm1 - O6	154.8 (2)	O7- Sm2- O3	154.7 (2)
Structure 2			
Cu1 - O1	1.9448(14)	Cu1 - O2	1.9437(14)
Cu1 - O1w	2.121(2)	Cu1 - Cu1	2.6283(6)
O1 - Cu1 - O1	88.67(10)	O1 - Cu1 - O2	167.90(6)
O2 - Cu1 - O2	88.58(10)	O1 - Cu1 - O1w	94.51(8)
O2 - Cu1 - O1w	97.60(8)		
Structure 3			
Zn1 - O7	1.953(2)	Zn1 - O5	1.999(3)
Zn1 - O1	2.006(3)	Zn1 - O8	2.112(3)
Zn1 - O4	2.127(3)	Zn2 - O6	1.911(3)
Zn2- O3	1.917(3)	Zn2 - O2	1.935(3)
Zn2 - O9	1.964(6)		
O7- Zn1- O5	121.35(12)	O7- Zn1 -O1	105.96(12)
O5- Zn1- O1	132.54(12)	O8- Zn1- O4	170.73(11)
O3- Zn2- O2	114.21(14)	O2- Zn2 -O9	110.8(4)

Table 3. Structural properties of the Zn, Cu and Sm MOFs. Accessible surface area A_{asa} , pore volume V_p , accessible volume, maximum pore size D_{max} , crystal density ρ_{cryst} , maximum calculated and measured drug loading and payloads (%wt).

System	A_{asa} (m ² g ⁻¹)	V_p (Å ³)	V_{acc} (cm ³ g ⁻¹)	D_{max} (Å)	ρ_{cryst} (g cm ⁻³)	Calc. loading (g/g)	Exp. loading (g/g)	%wt calc.	%wt exp
1 (SmMOF)	1815.3	16471.4	0.272	16.14	1.07	0.27	0.40	27.0	40.0
2 (CuMOF)	2163.3	1794.4	0.096	6.40	1.19	0.25	0.42	25.0	42.0
3 (ZnMOF)	2136.1	2594.7	0.366	12.30	0.95	0.28	0.45	28.0	45.0

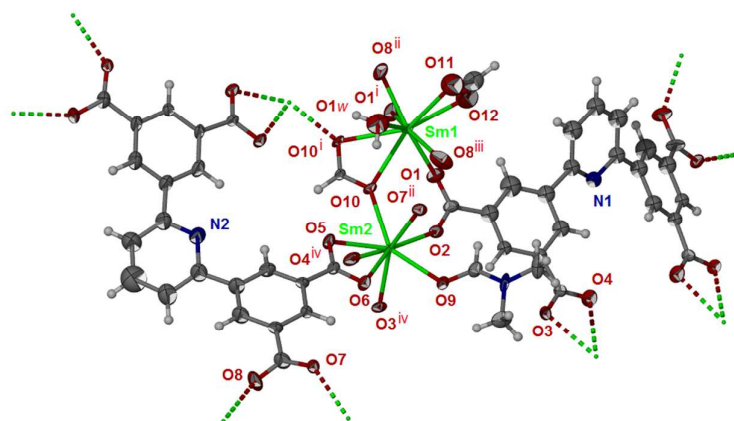


Figure 1. ORTEP plot of the coordination environment of Sm(III) ions and its connectivity L1 ligands in **1**, C grey, O red, N blue, Sm green. The uncoordinated water and DMF molecules are not shown (symmetric codes: (i) $x,-y,z$; (ii) y,z,x (iii) $x,-y,-z$; (iv) $x,y,-z$).

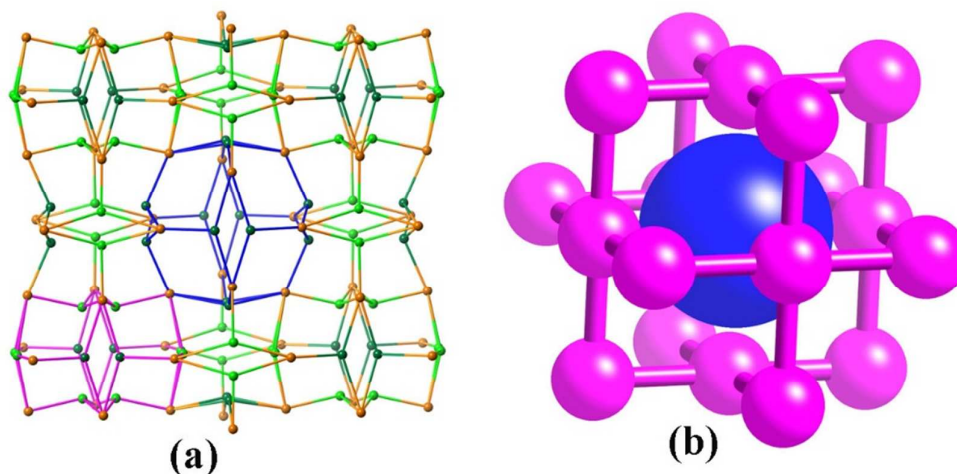


Figure 2. (a) Schematic representation of the 3D network formed in the structure of **1**. Light green and dark green nodes represent the two topologically different 3-connecting ligand nodes, while the orange nodes represent the 6-connecting Sm_3 clusters. A small cage is highlighted at the bottom right by the pink bonds; a large cage is highlighted in the centre by the blue bonds. (b) Schematic representation of the way the NbO -like arrangement of the smaller cages (blue sphere) generates the larger cages (pink sphere).

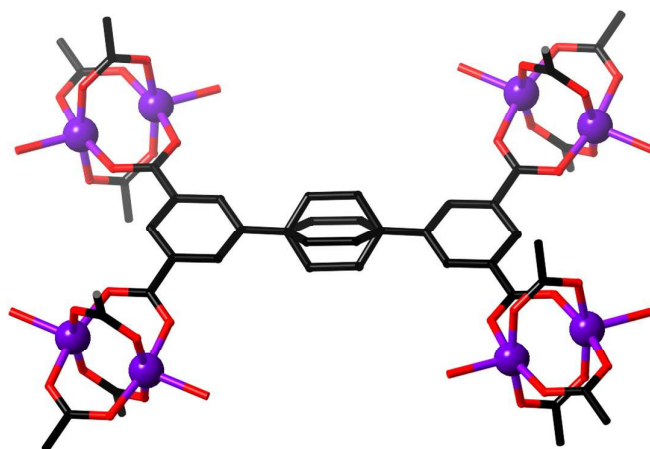


Figure 3. Local geometry of ligand and metal coordination environments in structure **2**, C black, O red, Cu pink. The central ring of the L2 ligand is disordered over two positions.

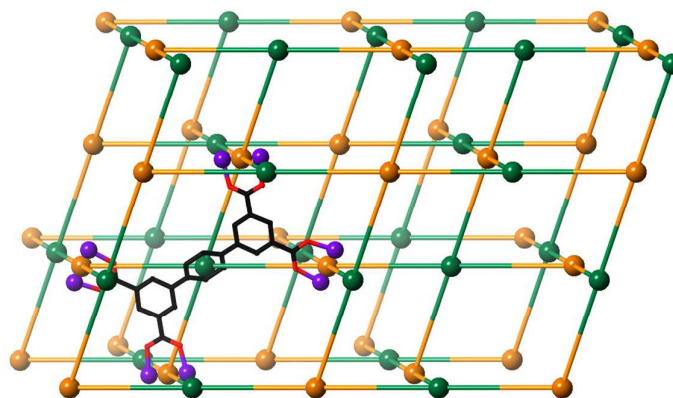


Figure 4. Schematic representation of the 3D NbO-like network in structure **2**. Green nodes represent the ligands, while the orange nodes represent the Cu₂ binuclear clusters. A single ligand of the chemical structure with coordinated Cu atoms is shown in the bottom left corner. For clarity, only one position of the disordered central ring is shown.

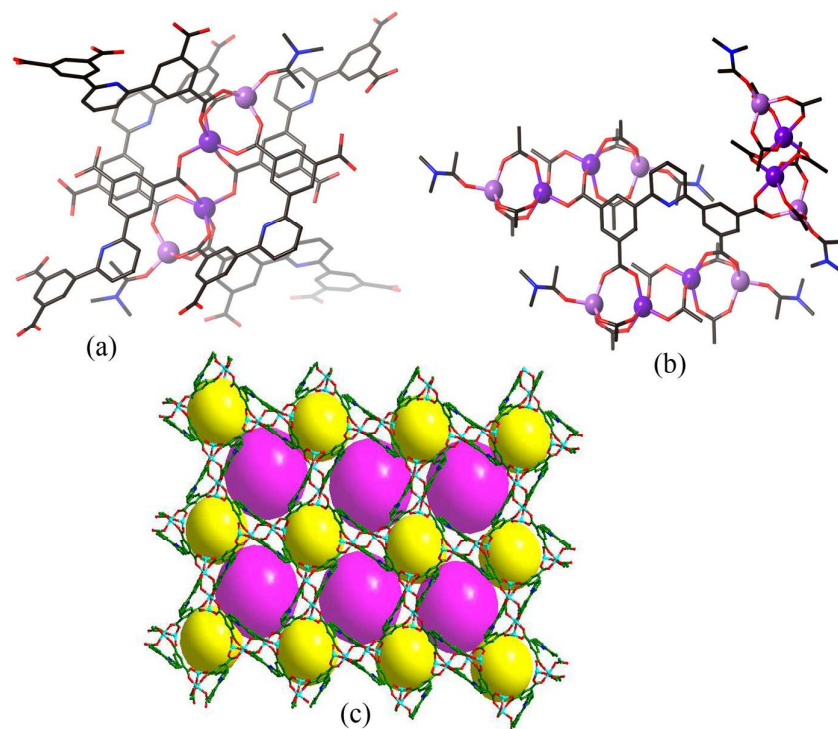


Figure 5. Local coordination geometries of (a) the Zn₄ cluster, and (b) the L ligand in the structure of **3**. C black, N blue, O red, Cu pink. For clarity, only one position of the disordered DMA ligand is shown, and (c) two kinds of nanoscale cages in **3**, the pink spheres represent the void space inside the large cages and the yellow spheres represent the small void space inside the small cages.

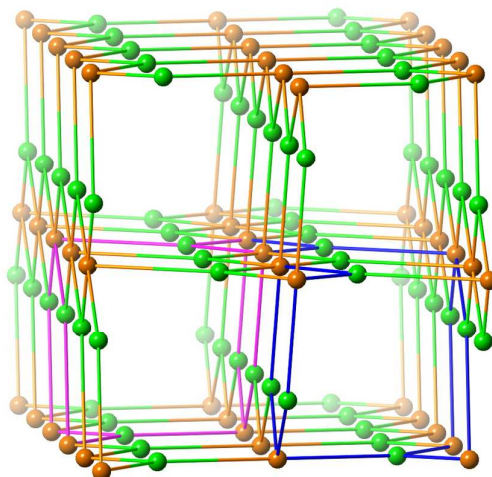


Figure 6 The underlying *zzz* net in the structure of **3**. Green nodes represent the 3-connecting ligands, while orange nodes represent the 6-connected Zn₄ clusters. Opposing 6-membered rings in a rutile-like channel are highlighted in pink; spiralling 6-membered rings in a helical channel are highlighted in blue.

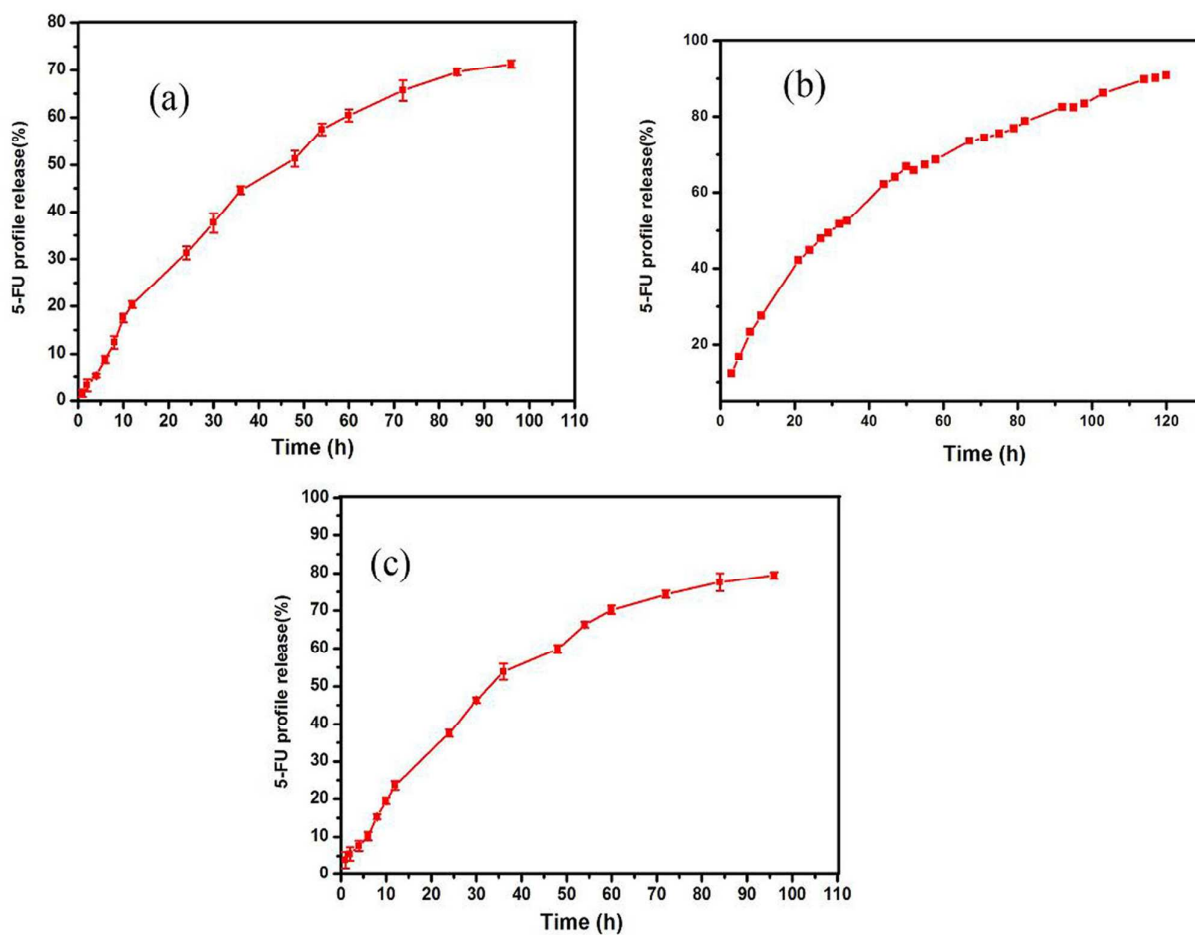


Figure 7. Release profile of the 5-FU from the drug-loaded materials 1-3 in PBS buffer at 37 °C as determined by UV-vis absorption spectroscopy (% 5-FU vs.time)

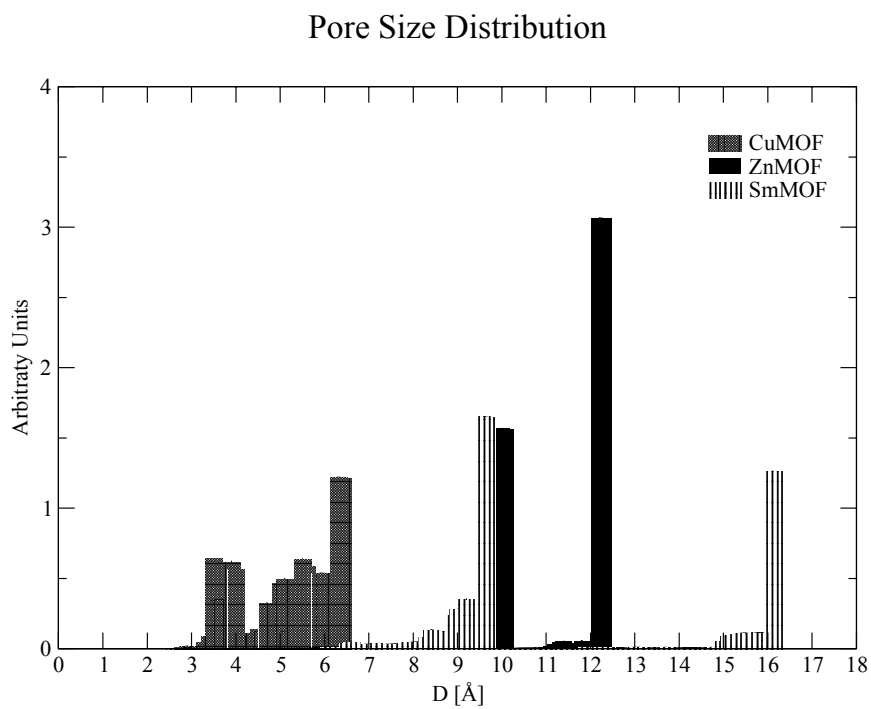


Figure 8. Pore size distributions for structures **1** (SmMOF), **2** (CuMOF) and **3** (ZnMOF).

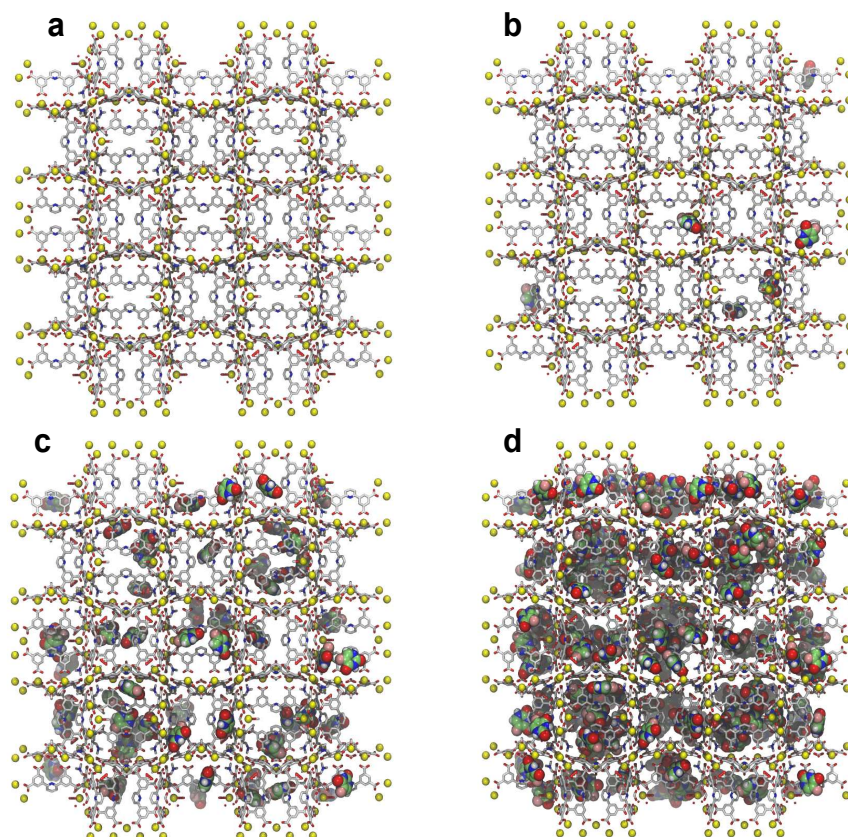


Figure 9. Sequential snapshots taken from the GCMC simulation of the adsorption of 5-FU into **1**. 5-FU atoms are shown in van der Waals representation (C in green, F in pink, N in blue, O in red and H in white). Atoms of the organic linkers of compound **1** are shown in licorice representation (C in white, O in red and N in blue). Yellow spheres represent the Sm atoms.

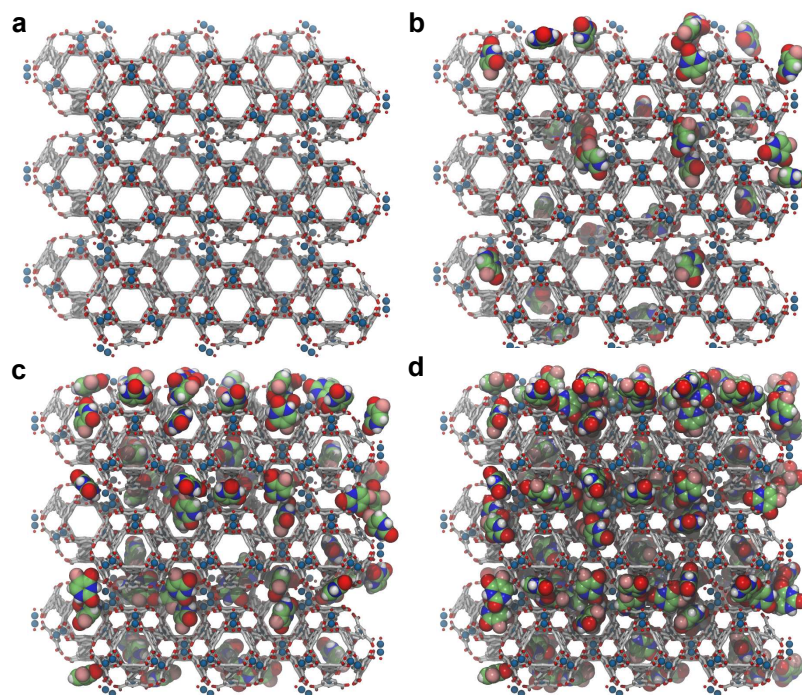


Figure 10. Sequential snapshots taken from the GCMC simulation of the adsorption of 5-FU into **2**. 5-FU atoms are shown in van der Waals representation (C in green, F in pink, N in blue, O in red and H in white). Atoms of the organic linkers of compound **2** are shown in licorice representation (C in white and O in red). Yellow spheres represent the Cu atoms.

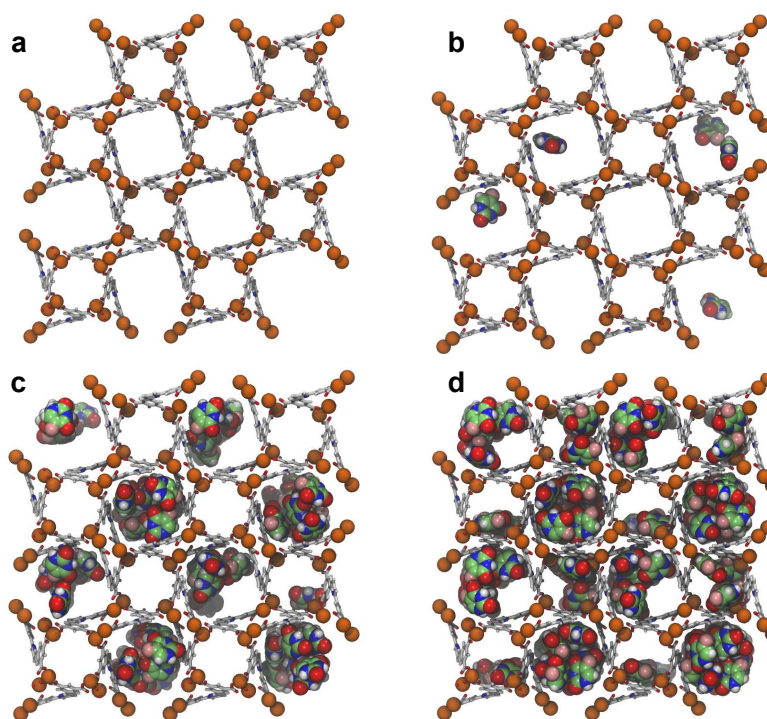


Figure 11. Sequential snapshots taken from the GCMC simulation of the adsorption of 5-FU into **3**. 5-FU atoms are shown in van der Waals representation (C in green, F in pink, N in blue, O in red and H in white). Atoms of the organic linkers of compound **3** are shown in licorice representation (C in white, O in red and N in blue). Orange spheres represent the Zn atoms.

